Beamforming for large-area scan and improved SNR in array-based photoacoustic microscopy

A. Cebrecos[a,*], J. J. García-Garrigós[a], A. Descals[a], N. Jiménez[a], J. M. Benlloch[a], F. Camarena[a]

[a] *Instituto de Instrumentación para Imagen Molecular (i3M), Consejo Superior de Investigaciones Científicas (CSIC), Universitat Politècnica de València (UPV), Camino de Vera s/n, 46022, Valencia, Spain.*

Abstract

Beamforming enhances the performance of photoacoustic microscopy systems for large-area scan. We present a detailed study quantifying and comparing SNR using different beamforming strategies to increase the field-of-view of optical-resolution photoacoustic-microscopy systems. The system combines a low-cost PLD with a 128-element linear ultrasound probe. Three beamforming strategies are analysed: a no-beamforming method equivalent to a single-element plane transducer, a static beamforming method that mimics a single-element focused transducer, and a dynamic beamforming applying a delay-and-sum algorithm. The imaging capabilities of the system are demonstrated generating high-resolution images of tissue-mimicking phantoms containing sub-millimetre ink tubes and an ex vivo rabbit's ear. The results show that DAS beamforming increases and homogenizes SNR along 1-cm^2 images, reaching values up to 15 dB compared to a no-beamforming method and up 30 dB with respect to out-of-focus regions of the static configuration. This strategy makes it possible to scan larger surfaces compared to standard configurations using single-element transducers, paving the way for advanced array-based PAM systems.

Keywords: Photoacoustic imaging, OR-PAM, array-based, DAS beamforming, large-area scan, pulsed laser diode

1. Introduction

Photoacoustic microscopy (PAM) is an imaging technique that combines optical excitation with ultrasound reception forming images from directly depth-resolved signals by raster-scanning the sample without applying reconstruction algorithms [1, 2]. It has received a growing interest over the last decade for its ability to provide anatomical, molecular, and functional imaging. As a short laser pulse is aimed at superficial biological tissue, some of the photons are absorbed by chromophores (oxyhemoglobin, deoxyhemoglobin, etc.) or exogenous contrast agents, inducing a local and fast temperature rise. As a result of the local thermoelastic expansion a pressure rise is produced leading to the generation of ultrasonic waves, a phenomenon known as the photoacoustic effect [3].

PAM is typically classified in two main categories, optical-resolution (OR-PAM) [4], based on the optical ballistic regime, and acoustic resolution (AR-PAM) [5], based on the diffusive regime. The lateral resolution of these two modalities is inherently different [1]. In OR-PAM, the laser excitation is tightly focused and hence, the size of the laser spot determines the lateral resolution,while in AR-PAM the lateral resolution is determined by the ultrasound system because the focal spot of the acoustic beam is smaller than the optical one, which is generally weakly focused. Resolution trades off with imaging depth [6, 7]: OR-PAM achieves better lateral resolution at the expense of a shallow penetration [8, 9], whereas the opposite occurs in AR-PAM [10].

For the light source, OR-PAM typically uses different types of short-pulsed solid state lasers, such as Nd:YLF [4], Nd:YAG [7], Nd:YV04 [8], or even Ti:Sapphire [11]. They provide short pulses and high energy per pulse, although they generally have a high cost, large size and require a bulky cooling system. Moreover, the repetition rate may be relatively low [12]. As an inexpensive and more compact alternative, pulsed laser diodes (PLD) [13–18] or light emitting diodes (LED) [19–21] are often employed (see Ref. [22] for a thorough review on low-cost sources). Their main drawback is their poor signal-to-noise ratio (SNR) which usually requires multiple averaging.

Regarding ultrasound detectors, conventional OR-PAM systems rely on piezoelectric transducers or optical-acoustic detectors (such as Fabry-Perot ultrasound sensors) [6]. Many piezoelectric-based OR-PAM systems use focused single-element transducers with focal spots of very few mm^2, often submerged in water or other fluids that allow relative displacement between sample and probe, resulting in relatively small images. Conversely, optical-acoustic detectors with improved sensitivity and wide acceptance of angles have been proposed as good candidates to increase the field-of-view (FOV) of photoacoustic images, such as detectors based on fibre optic sensors [23, 24].

Array-based PAM systems were initially proposed with different goals: As a way to leverage the ultrasound probe present in US array systems, as demonstrated by Wang and co-workers in their implementation for guiding needle biopsy of sentinel lymph nodes in rats [25], or Merhmohammadi and co-workers,

*Corresponding author
Email address: alcebrui@upv.es (A. Cebrecos)

who proposed a miniaturized array-based photoacoustic endoscopic imaging system designed for volumetric dual-modal US and PA images [26]; to take advantage of the in-depth dynamic focusing capability of ultrasound arrays to form volumetric images [27, 28]; or to improve the imaging speed for obtaining real-time imaging systems [29–32]. Hajireza et al. reported an array-based optical resolution photoacoustic microendoscopy system composed of a fibre laser and a 128-element ultrasound linear array. With the acquired signals, they later performed delay-and-sum (DAS) beamforming to produce small images (< 1 mm^2) of the vasculature of the ear of a rat [33]. Zheng and co-workers applied DAS beamforming within the surface of the imaging plane, showing the SNR improvement when using a 64-element phased array compared to images obtained using only one element of the phased array [34]. However, the capabilities of DAS beamforming within the imaging plane to increase the FOV and SNR with respect to other standard configurations, i.e., single-element plane or focused transducers, remains unexplored.

In this work, we study the performance of several beamforming strategies to generate large area images in an array-based OR-PAM system using a low-cost PLD laser as the excitation source. We show that DAS beamforming makes it possible to greatly increase and spatially homogenize the SNR of the image, especially in out-of-focus regions, compared to other PAM configurations featuring single-element ultrasonic transducers. In addition, the use of DAS beamforming avoids the need to displace the ultrasound probe with respect to the imaged sample. Images of sub-millimetre polyethylene tubes filled with India ink embedded in tissue mimicking phantoms and the microvasculature of an ex vivo rabbit ear were acquired in order to evaluate the performance of the system. A detailed laser beam spot characterization was performed by both optical and acoustical means yielding a lateral resolution of 200 x 119 μm^2, while the experimental results of the developed PAM system demonstrate a spatially homogenized SNR increase up to nearly 30 dB for out-of-focus regions along a large area scan of around 1 cm^2, compared to a classical static focus configuration.

2. Materials and methods

2.1. *Laser diode excitation and beam optics configuration*

A high-power PLD of 650 W output peak power and 905 $\pm$ 10 nm central wavelength was used (model 905D5S2L3J08X, Laser Components, Germany). As depicted in Fig. 1, the laser diode is driven by forward current pulses from a variable voltage driver module (LDP-V 80-100, PicoLAS, Germany) in order to produce a burst of optical power pulses at a 2 kHz repetition rate and 100 ns pulse width (0.02% duty cycle) during a given excitation time. The PLD pulsed operation was set to a safe and non-destructive regime well below its absolute maximum ratings of 150 ns pulse width and 0.1% duty cycle. The laser diode driver is first configured from a dedicated microcontroller-based board, which sets the laser diode output power, ranging linearly from the laser threshold up to the maximum optical for the driver voltages 23–100 V; and also monitors safe operation settings like temperature and voltage limits. Afterwards, it runs as a signal-follower of the square pulse train sent by the pulse generator to the driver input signal port. Timing synchronization between the ultrasound DAQ system and PLD output pulses is achieved through a TTL trigger signal generated by the ultrasound system to the pulse generator.

The PLD is a mini-stack of 30 single-emitters arranged in 2 columns with 5 bars of 3 emitters each, which results in a structured light pattern emitted from a whole rectangular area of 800×440 μm^2. It emits an elliptic and relatively high divergent beam with full-angle divergence of 10° and 25° for the horizontal (slow axis) and vertical (fast axis) planes, respectively. The PLD beam quality for each plane is $M^2 \approx (121, 166)$, which can be determined from the well-known relation $BPP = M^2\,(\lambda/\pi)$ for its nominal wavelength $\lambda = 905$ nm and $BPP \approx (35, 48)$ mm mrad, the beam-parameter product of the emitting surface radius and half-divergence, $BPP \equiv \mathrm{w}_0\,\theta$. Laser diode stacks have in general high M-squared values, much greater than a diffraction-limited beam $M^2 >> 1$ due to their inherently multimodal emission, which will limit the smallest beam spot size achievable by any optics, and ultimately the lateral resolution of OR-PAM imaging systems.

The optics scheme used to deliver and concentrate the laser beam power from the PLD into a small spot excitation area inside the imaging target (phantom or tissue) is shown in Fig. 1. The PLD optics comprises two plano-convex aspheric lenses, both with suitable anti-reflection coatings in the NIR range. A first lens of $f_1 = 20.1$ mm focal length, a diameter of 25 mm and high numerical aperture NA=0.6 (ACL2520U-B, Thorlabs), is used to collect and collimate, or pre-focus, the light from a highly divergent beam emitted by the PLD stack. A second lens of shorter focal length of $f_2 = 10.5$ mm, with 12 mm on diameter and NA=0.54 (ACL1210U-B, Thorlabs), focalises the laser into a small spot area corresponding to the beam waist at the focus of this two-lens optical scheme. The aperture stop of this configuration is limited to the clear aperture of the focusing lens CA=10.8 mm. The distances for this optical configuration were set to: $s_1 = 50$ mm from the laser diode emitting surface to the collimating lens object principal plane H_1, and $s_2 = 11$ mm from there to the focusing lens image principal plane H_2'. The working distance (WD) is defined from the last lens mount surface to the focused beam waist giving thus the usable laser excitation depth inside the target volume, as depicted in the optical schematic of Fig. 1. After simulations of this optical configuration, based on both ray-tracing and M-squared-corrected Gaussian optics, the WD for our setup was set to 2.3 mm on air, and 3 mm on water (with refractive index $n = 1.33$). Note that the WD from the lens backplane would be longer but it is shortened by the lens mount fixing ring of 1.7 mm width.

The laser power distribution cross-section at the beam focus was obtained in order to better determine the beam spot size and also the power eventually delivered to it, as presented later in Section 3.1. A cross-section image at the focal plane was acquired from ray-tracing simulations to be analysed and compared to a measured image of the focus taken with a beam profiler CCD camera (LT665, Ophir, Israel) and a 60 mm focal lens in a $4f$-imaging configuration with magnification one-to-one.

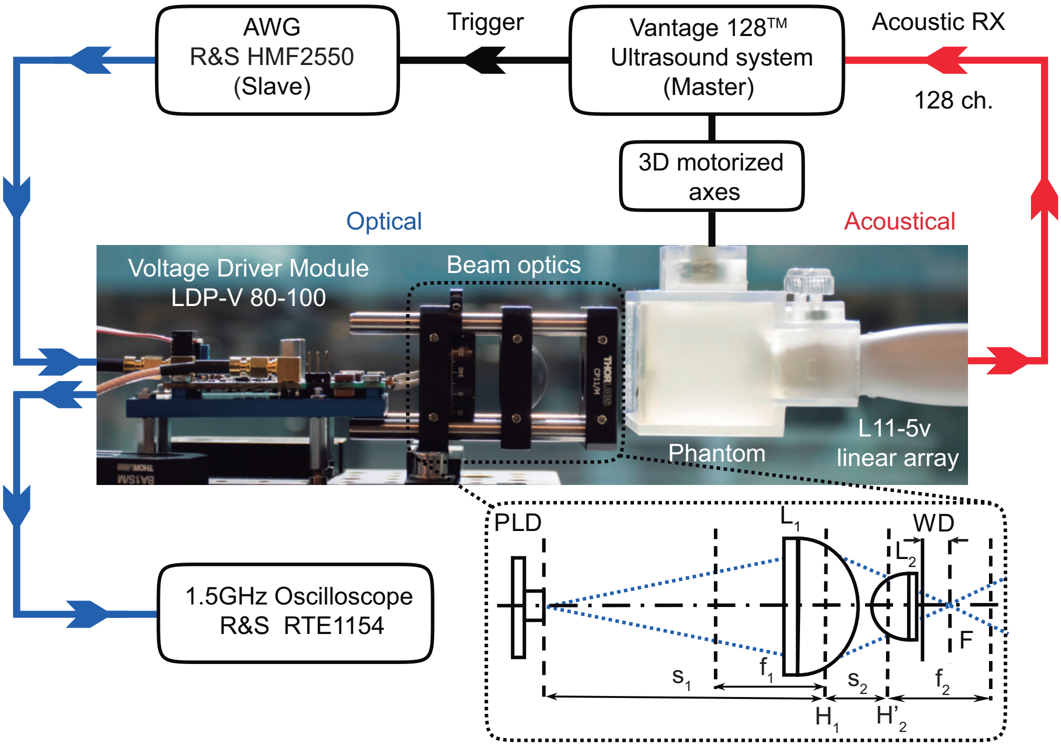

Figure 1: **Schematic diagram and main building blocks of the PAM system**. Blue arrows refer to the signals of the optical part, starting from the arbitrary waveform generator to the driver and oscilloscope, while red lines represent the received acoustic signals from the ultrasound probe to the Vantage system, which acts as the master and controls trigger, emitted and received signals, as well as the mechanical rastering of the sample. A detailed beam optic diagram is included describing the PLD optical configuration for focusing the laser beam at the focusing plane (F).

The beam spot size given by optical means can then be compared to the beam spot size measured from the photoacoustic images, applying in the Edge Spread Function (ESF) method, as a way of cross-checking and validate both imaging measurements.

The beam power delivered at the focal plane was measured with a calibrated integrating sphere (AvaSphere-30) into a 6-mm diameter aperture port, connected by a fibre optical cable (FC-UVIR600-1-ME) to a Czerny-Turner monochromator spectrometer (AvaSpec-ULS2048XL-EVO) with 1.5 nm spectral resolution, being all these elements from Avantes, Netherlands. This measurement was then used in the simulation to calibrate the power distribution image at the same focal plane, so that the power delivered into a delimited spot area was estimated more accurately. The PLD emission wavelength and its bandwidth were also measured from the acquired laser spectrum.

2.2. *Ultrasound detection and beamforming*

As illustrated in Fig. 1, the system uses a transmission mode configuration where the incident light and the US reception are located at opposite sides of the sample. The ultrasound acquisition system is a Vantage 256^{TM} (Verasonics, USA) connected to a 128-element linear US probe (L11-5v, Verasonics, USA). The Vantage system generates the TTL trigger signal that synchronizes the arbitrary waveform generator that sends the electrical pulses to the Voltage Driver Module and PLD. Acoustic signals are collected across all 128 elements simultaneously at a PRF of 2 kHz and averaged 256 for the gelatin phantom experiments and 512 for ex vivo experiments. The ultrasound probe is acoustic-impedance matched to the phantom using coupling gel. Gelatin-based phantoms were produced inside a custom-made plastic container using 6% m/V of gelatin 200-220 bloom, adding 0.1% m/V of formaldehyde to increase long-term stability [35]. Hollow polyethylene tubes (0.85 mm out-diameter, 0.42 mm in-diameter) filled with India ink were inserted close to the surface of the gelatin to simulate blood vessels. The phantom container was attached to a 3D scanning motor for positioning and raster-scanning of the sample in a two-dimensional plane perpendicular to the laser beam at its focusing plane.

RF-signals corresponding to each of the channels at every scanned point were registered. Data is later processed in a MATLAB (Mathworks, USA) environment in order to generate maximum intensity projection (MIP) images. Three different beamforming strategies were followed to illustrate and quantify the advantages of the dynamic beamforming. First, a no-beamforming approach in which, for every scanning point, signals are directly summed up without taking into account the delay between the ultrasound wave and the position of each element of the array, a behaviour analogous to what a single-element plane transducer would present. Second, a static beamforming strategy where all 128 signals are combined in order to have a fixed focusing position in reception for every scanning point, which imitates a single-element focused transducer placed at a fixed position. Finally, we evaluate the performance of a DAS beamforming strategy, where the focusing is dynamically repositioned at every measured point to match the location of the laser excitation. For a given scan position, the output signal using the DAS algorithm reads

$$y_{DAS}(t) = \sum_{i=1}^{N} y_i(t - \Delta_i) \quad (1)$$

where $N = 128$ is the number of elements of the ultrasound probe, $y_i(t - \Delta_i)$ is the signal received by the i-th channel of the array considering its corresponding delay Δ_i, which is obtained as the three-dimensional distance between the position of the laser focus within the focusing plane F, and the position of the i-th element of the array, assuming a speed of sound $c = 1540$ m/s.

3. Results

3.1. Laser beam focus characterization

The laser beam energy distribution delivered at the focal plane was first obtained by ray-tracing simulation of the optical configuration (Fig. 1). The simulation was implemented considering the total power emission from the PLD stack source, as an array of single laser diode emitters according to the manufacturer geometrical and optical specifications; followed by the optics set, with their specific aspheric lens geometries, NIR anti-reflection coatings and corresponding mount apertures. Figure 2 (a) shows the simulation output image of the laser beam pattern within a 1×1 mm^2 area at the focusing plane position, which corresponds to a working distance of 2.3 mm and divergence of around 22° and 45° for horizontal and vertical planes, respectively. This simulation allowed us to make a good estimation of the energy delivered into any region of the beam focusing plane, after performing an energy calibration in order to get the fluence map of the simulated image (in mJ/cm^2 units).

For that purpose, a measurement of the total power was performed using the spectrometer and integrating sphere, where its sample port is just placed at the beam focusing plane of the optics setup. A total power of 300.5 W was measured over the 6 mm diameter sample port, and then applied to the same aperture area in the simulated beam power distribution, yielding a total energy of 30.05 μJ in this area for the laser pulse width $\tau_p = 100$ ns. The power measurement was eventually performed in the spectrometer by averaging 1000 energy pulses acquired for a 10 ms time integration window per pulse, and after integrating the full spectrum, with measured central wavelength and bandwidth of 907 ± 7 nm, in agreement with the laser specifications.

As a result, the laser pulse energy delivered at the focusing plane could be more accurately estimated from the calibrated fluence map shown in Fig. 2(a), being 21.7 μJ for a 1×1 mm^2 fluence map image size and 10.7 μJ for the laser rectangular spot area 200×119 μm^2 (overlaid in the fluence map image with one pixel size error of 4.54 μm), as it was measured by photoacoustic means using the ESF presented in the following section. A PLD peak emission power of 510 W was also measured for several optical configurations with the integrating sphere, which approximately match to maximum forward current given by the PLD driver at around 45 A. This means laser power transport efficiencies of 68% for the setup optics into the focusing plane, and a 54% for the power delivered to the beam spot area.

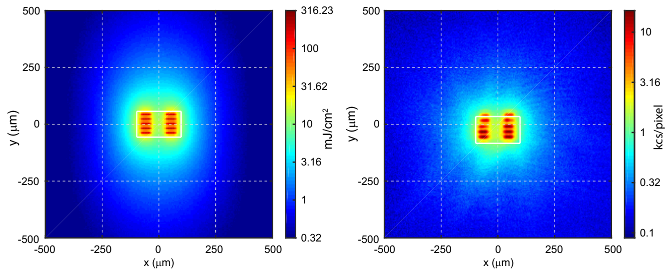

Figure 2: **Laser energy distribution at its focusing plane.** (a) Ray-tracing simulation. (b) Experimental measurement with a CCD camera and a $4f$-imaging lens.

The simulated beam pattern image is also compared to the experimental image of the beam focus pattern shown in Fig. 2 (b) which was taken with a 60 mm focal lens and a CCD NIR camera at $4f$-imaging distance from the PLD focusing plane with 1:1 magnification. The acquired image size is 224×224 pixels for the camera set to 1×1 mm^2 aperture and having 4.54 μm pixel size. Due to the high sensitivity of the CCD detector a set of neutral density filters were applied to attenuate light by a factor 10^{-6}. Synchronization for triggering the camera, at its minimum 30 μs exposure time, was directly performed from the pulse train signal from function generator driving also the PLD driver. Note also that the beam focus image is not calibrated and thus shown in counts per pixel units. In this case it was not possible to perform an experimental energy calibration, since the power arriving to the camera detector after the imaging lens does not conserve proportionality with respect to the power at the object focusing plane. This is mainly due to some spatial filtering made by the imaging lens over the highly divergent beam exiting after the focusing plane.

3.2. Lateral resolution: Edge Spread Function

The lateral resolution of the PAM system, defined by the laser beam spot size, was characterized from both optical and acoustical experimental measurements, as shown in Fig. 3. First, data from the optical characterization of the laser beam focus shown in Fig. 2 (b), was extracted and averaged for every horizontal and vertical line along the $x-y$ plane within the rectangular spot area to obtain one single line for each orientation, as shown in Figs. 3 (a, b). The beam spot size of this complex profile is defined by taking the full-width at half-maximum (FWHM) from a Gaussian fit (solid blue lines), as a first order approximation of the more complex power profile. The resulting measurement of the PLD optical beam excitation spot was 222×127 μm^2. Similar results were obtained for the simulated data, shown in Fig. 2 (a), with an estimated spot size of 217×112 μm^2. For the acoustical characterization, we made use of the edge spread function estimation considering the different horizontal and vertical properties of the PLD beam profile.

A highly absorbing 180-μm black vinyl strip was embedded in the phantom at around 1 mm beneath its surface and partially imaged, as shown in the insets of Figs. 3(c, d). The scanned area was 2×2 mm^2 for both horizontal and vertical orientations, with step increments of 10 μm, and the detected signals were averaged 256 times. The laser diode driver was set to half of its maximum range (at 50V), which means that an optical power of 150 W was eventually delivered to the focal excitation region, as obtained from linear calibration of the previous laser power measurement. The measured photoacoustic profile lines are shown as solid black lines in Figs. 3(c, d) for the horizontal and vertical orientations, respectively. A representative trajectory of the measured profiles is shown in the insets by red dotted lines. All measured profiles within the imaged area were averaged to obtain a single ESF. Their respective spatial derivatives, i.e., linear spread functions (LSF) were fitted using a Gaussian function. The lateral resolution extracted from the FWHM of the fitted curve was 199.8 μm and 118.9 μm for the horizontal and vertical orientations, respectively. The laser pulse energy within the lateral resolution spot area would be of 5.3 μJ, which means an average fluence of 222 mJ/cm^2, as determined from previous laser energy estimations.

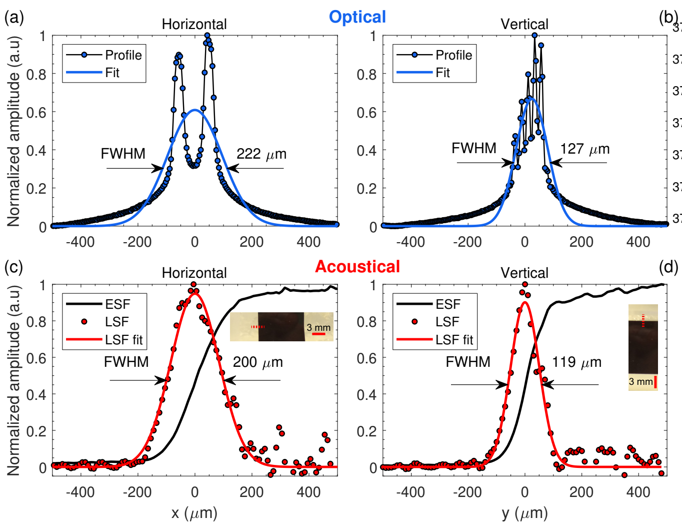

Figure 3: **Lateral resolution evaluation**. (a) Horizontal and (b) vertical optical *x-y* experimental profiles of the laser beam at its focus and beam spot size from Gaussian fitting at FWHM. (c) Horizontal and (d) vertical ESFs, LSFs and corresponding Gaussian fittings obtained from photoacoustic measurements.

The beam spot sizes measured by optical and acoustical methods show a good agreement between them. This seems to indicate that in the photoacoustic interaction, where the laser energy is converted into a thermoelastic expansion after heating the targeted material, a smoothing of the spikes of the underlying laser distribution is produced, possibly due to the integration of the laser energy density (fluence or intensity) when it is absorbed by the material.

3.3. *Gelatin phantoms 2D imaging*

To evaluate the performance of the PAM system and graphically show the differences between the different beamforming strategies we first took 2D large-area images of gelatin phantoms including polyethylene tubes filled with India ink (inner diameter 0.42 mm, outer diameter 0.85 mm). The scanned area was nearly 1 cm^2 (1.2 cm $\times$ 0.8 cm), using step increments of 50 μm, resulting in images having 39862 pixels. Registered signals were averaged 256 at every point of the image. As previously determined, the laser excitation corresponds to 5.3 μJ pulse energy and 222 mJ/cm^2 average fluence in the focus spot area. Figure 4 (a) illustrates a photograph of the phantom and highlights the imaged area.

Following the acquisition of the RF-signals for all 128 channels of the ultrasound probe at every point of the image, data was processed and summed-up differently according to the three proposed beamforming strategies. First, for the no beamforming strategy, data from every channel were directly summed up (see Fig. 4 (b)). Then, for the static beamforming strategy, time delays for every channel were calculated in order to point the focus in reception at the point $(2, 0)$ mm, and time signals were time-shifted accordingly (Fig. 4 (c)). Finally, for the dynamic beamforming strategy, the focal law in reception was set to match the location of the imaged pixel using the DAS algorithm, (Fig. 4 (d)). Once the beamforming strategy was applied, the photoacoustic image was obtained by considering the MIP, plotting the result in logarithmic scale. These results clearly indicate that if a large-area image is desired, neither the no-beamforming nor the static beamforming strategies can provide sharp images, failing to achieve enough and uniform contrast for the whole scanned area. On the other hand, when applying a dynamic beamforming strategy, the SNR along the imaged area is greatly homogenized and increased around 20 dB, enhancing the overall contrast.

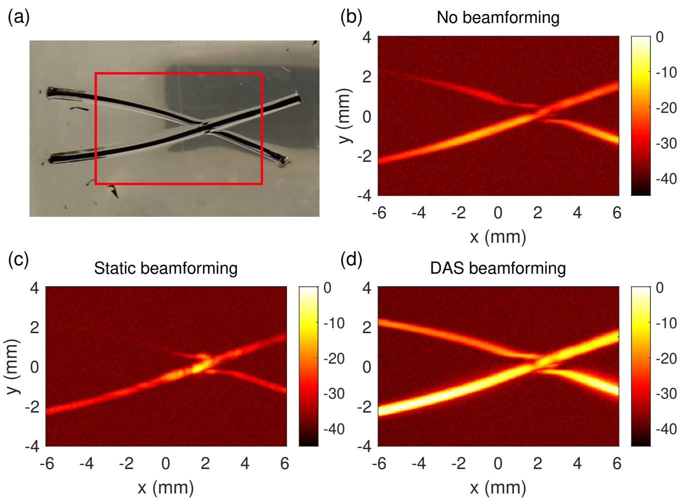

Figure 4: **2D photoacoustic images using gelatin phantoms.** (a) Photograph of the surface of the phantom including polyethylene tubes at its surface. The red rectangle represents the scanned area. 2D photoacoustic images of the gelatin phantoms using a single set of experimental data, applying (b) no-beamforming, (c) static beamforming aimed at the crossing point of the PE tubes and (d) dynamic beamforming aiming the focusing point at the focal spot of the laser for every scanned point.

An additional photoacoustic experiment was performed to better quantify the differences between the three beamforming strategies. A single polyethylene tube filled with India Ink was located inside a gelatin phantom nearly at its surface in a quasi-horizontal position, i.e., aligned to the x-axis. Note that since the ultrasound array is a 1D probe, the dynamic focusing strategy is only feasible along the x-axis and z-axis. The scanned area for this experiment was 0.6 cm^2 (2 cm $\times$ 0.3 cm), using step increments of 50 μm, for a total of 24862 pixels (401 $\times$ 62). As before, 256 signals were averaged at every point of the image with 5.3 μJ of laser pulse energy and 222 mJ/cm^2 of fluence per point. A photograph of the sample is shown in Fig. 5 (a). Photoacoustic images extracted from MIP of the processed time series signals are shown in Figs. 5(b, c, d) for all three beamforming strategies. Finally, Fig. 5 (e) represents the comparison of SNR along the horizontal x-axis at the y point corresponding to the centre of the tube.

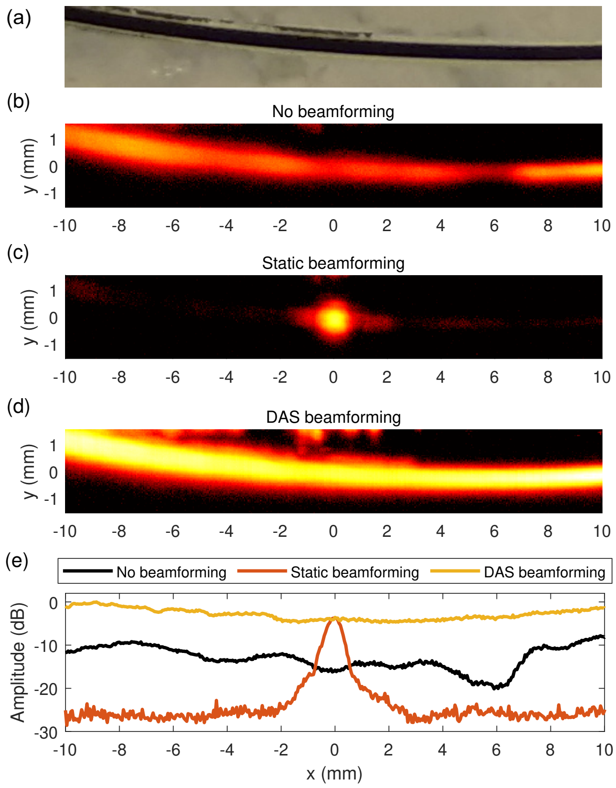

Figure 5: **SNR comparison between beamforming strategies.** (a) Photograph of the gelatin phantom featuring an India Ink filled PE tube. 2D photoacoustic images using (b) no beamforming, (c) static beamforming, and (d) dynamic beamforming. (e) SNR comparison along the x−axis at the centre of the tube.

Results shown in Fig. 5 (e) represent a clear picture of the difference in performance between the three beamforming strategies. First, for the sake of consistency, note that the static and dynamic beamforming strategies have the same SNR when evaluated at the focus of the former. The dynamic beamforming strategy offers a quite homogeneous SNR along the polyethylene tube for almost 2 cm, with variations below 3 dB. Moreover, this small variations are influenced by small differences in the depth along the z-axis of the tube, considering its size with respect to the depth of field of the laser at its focus (approximately 1 mm). When comparing these results with a no-beamforming strategy, there exists an overall reduction of 10 to 20 dB in SNR. If compared to the static beamforming strategy, the SNR increase nearly reaches 30 dB for out-of-focus regions.

3.4. Rabbit ear 2D imaging

To evaluate the performance of the proposed PAM system in a more realistic environment, ex vivo images of a rabbit's ear were taken. Rabbit ears were provided by the Instituto de Ciencia Animal (ICTA) of the Universitat Politècnica de València (accredited animal care facility ES462500001091) in agreement with European legislation. Two strategies (no-beamforming and dynamic beamforming) were considered for the same set of experimental data. The scanned area was 0.72 cm^2 (1.2 cm $\times$ 0.6 cm), using step increments of 50 μm, resulting in images having 29282 pixels. Since the optical absorption coefficient for blood at the working wavelength is around 10 cm^{-1}, more than one order of magnitude lower than for India ink, which is around 200-400 cm^{-1} [1, 35], the number of averages when imaging the rabbit ear was increased to 512 laser pulse shots at the same excitation energy of 5.3 μJ and 222 mJ/cm^2 fluence per image point. A photograph of the rabbit's ear including a rectangle indicating the scanned area and the corresponding photoacoustic images using the two beamforming techniques are shown in Fig. 6. The obtained results highlight the relevance of the dynamic beamforming, shown in Fig. 6(c), not only to homogenize the SNR along the scanned area, but most importantly, in this case, to discern different elements of the rabbit ear's vasculature, which are hardly visible for the no-beamforming case shown in Fig. 6 (b). Beamformed image highlights the presence of several capillaries of different size and allows to see details that are even hardly visible by a direct visualization of the photograph shown in Fig. 6 (a). Note that the SNR improvement obtained in this experiment is consistent with the results presented previously for the phantom, where the improvement was between 10 and 20 dB.

4. Conclusions

In this work, we have compared different beamforming strategies in terms of signal-to-noise ratio with an array-based photoacoustic microscopy system. We demonstrate that DAS beamforming allows to greatly extend the imaging area of photoacoustic images. In addition, the signal-to-noise ratio is increased and spatially homogenized along the imaging plane. In particular, we utilized a low-cost PLD controlled by a voltage driver module and combined with an optics scheme composed of two plano-convex aspheric lenses as the laser excitation, achieving a rectangular focal spot of 200 $\times$ 119 μm^2 and a pulse energy ranging from 3.2 to 10.7 μJ, for a fluence within the laser focal spot between 134 and 450 mJ/cm^2. The lateral resolution of the system was characterized from both optical and acoustical measurements based on the edge spread function method, obtaining a very good agreement between them. Images of polyethylene tubes filled with India ink embedded in tissue-mimicking phantoms comparing different beamforming techniques demonstrated the benefits of applying dynamic

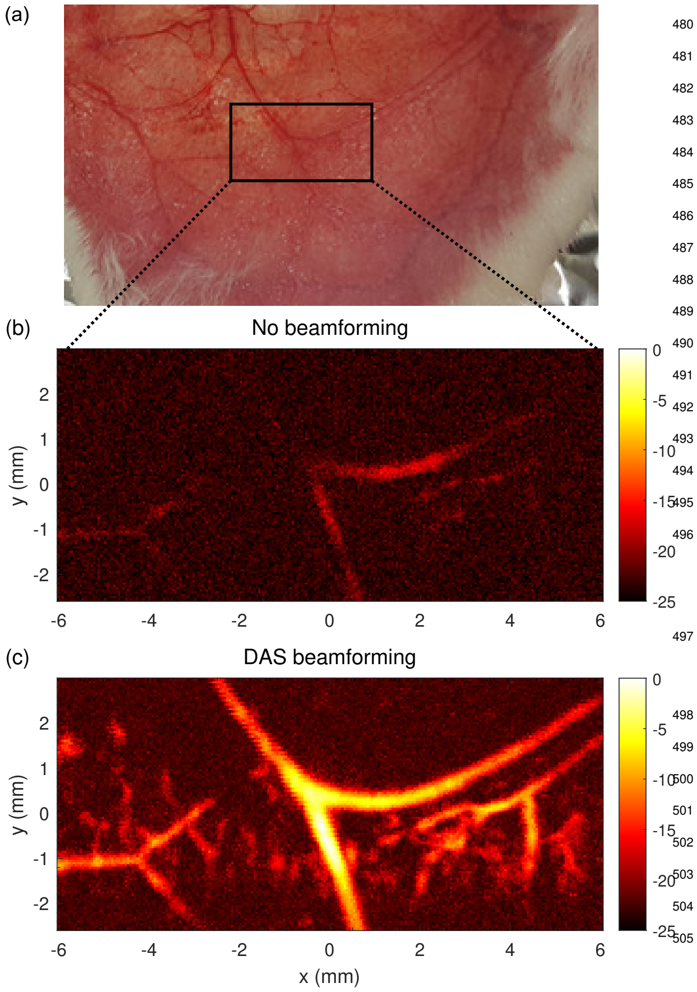

Figure 6: **Ex vivo rabbit ear 2D PAM imaging.** (a) Photograph of the excised rabbit ear, where the black rectangle indicates the scanned area. PAM images of the rabbit ear vasculature comparing (b) no-beamforming and (c) dynamic beamforming.

beamforming in the imaging plane to form very large areas (around 1 cm^2 and nearly 40000 pixels) with an improved and homogenized SNR along the whole imaged area, reaching improvements up to nearly 30 dB compared to a static focus configuration. Finally, ex vivo large-area images of the microvasculature of the ear of a rabbit were taken, observing the presence of capillaries of different sizes, obtaining similar SNR improvements when applying dynamic beamforming as those using gelatin phantoms, and therefore validating these results in a more realistic environment.

One of the advantages of DAS beamforming in OR-PAM systems is that the ultrasound probe and the imaged sample can be physically coupled, allowing fast scanning during large-area imaging for in vivo applications. Regarding the obtained SNR improvements using DAS beamforming, note that advanced beamforming algorithms such as DMAS, DS-DMAS, F-DMAS [36–38], sparsity-based beamforming [39], eigen-space based minimum variance [40], or even sinthetic aperture focusing techniques [41, 42] could be applied to further enhance SNR in the present OR-PAM system.

In addition, large-area scan images are limited by the required scanning times, which ultimately depend on the PRF of the laser, but also on the scanning method and number of averages. Although real-time imaging of large areas might still be difficult to achieve in OR-PAM because imaging speed is ultimately limited by the acoustic wave propagation in soft tissues, imaging large areas within a few minutes is still feasible with the existing technology. In this regard, the imaging speed can be improved dramatically by using higher PRFs combined with fast laser scanning methods such as micro-electro-mechanical systems (MEMS) or galvanometer-based scanning methods. In these configurations, the dynamic beamforming techniques reported in this work can be applied to synchronise the alignment between the optical and acoustical focal spots during large-area scans, improving and homogenizing the signal-to-noise ratio of photoacoustic microscopy images for practical biomedical applications.

Author contributions

Conceptualization, A.C., J.J.G.G, N.J, J.M.B and F.C.; Data curation, A.C., J.J.G.G. A.D; Funding acquisition, F.C. J.M.B; Software, A.C., J.J.G.G, A.D. and N.J.; Writing–original draft preparation, A.C and J.J.G.G.; writing–review and editing, A.C., J.J.G.G, A.D, N.J, J.M.B and F.C.; Supervision, A.C., J.J.G.G, N.J, J.M.B and F.C.; project administration, J.M.B and F.C.; All authors have read, critically reviewed and agreed to the final version of the manuscript.

Funding

This research has been supported by the Spanish Ministry of Science, Innovation and Universities through grant “Juan de la Cierva - Incorporación” (IJC2018-037897-I), and program ”Proyectos I+D+i 2019” (PID2019-111436RB-C22), by Programa Operativo Empleo Juvenil 2014-2020 (MIN19-VAL-I3M-004), and by the Agència Valenciana de la Innovació through grant INNCON00/2020/009. Action co-financed by the European Union through the Programa Operativo del Fondo Europeo de Desarrollo Regional (FEDER) of the Comunitat Valenciana 2014-2020 (IDIFEDER/2018/022). A.C. received financial support from Generalitat Valenciana and Universitat Politècnica de València through the grants APOSTD/2018/229 and program PAID-10-19, respectively. AD received support from Generalitat Valenciana through grant GJIDI/2018/A/249.

Acknowledgements

We would like to thank Francisco Marco Jiménez of the ICTA at the Universitat Politècnica de València, who provided the ex vivo samples as well as useful guidance on the handling and proper conservation of the specimens.

References

[1] J. Yao, L. V. Wang, Photoacoustic microscopy, Laser & photonics reviews 7 (5) (2013) 758–778.

[2] S. Jeon, J. Kim, D. Lee, J. W. Baik, C. Kim, Review on practical photoacoustic microscopy, Photoacoustics 15 (2019) 100141.

[3] P. Beard, Biomedical photoacoustic imaging, Interface focus 1 (4) (2011) 602–631.

[4] K. Maslov, H. F. Zhang, S. Hu, L. V. Wang, Optical-resolution photoacoustic microscopy for in vivo imaging of single capillaries, Optics letters 33 (9) (2008) 929–931.

[5] K. Maslov, G. Stoica, L. V. Wang, In vivo dark-field reflection-mode photoacoustic microscopy, Optics letters 30 (6) (2005) 625–627.

[6] J. Yao, L. V. Wang, Sensitivity of photoacoustic microscopy, Photoacoustics 2 (2) (2014) 87–101.

[7] L. V. Wang, J. Yao, A practical guide to photoacoustic tomography in the life sciences, Nature methods 13 (8) (2016) 627.

[8] C. Zhang, K. Maslov, L. V. Wang, Subwavelength-resolution label-free photoacoustic microscopy of optical absorption in vivo, Optics letters 35 (19) (2010) 3195–3197.

[9] S. Hu, K. Maslov, L. V. Wang, Second-generation optical-resolution photoacoustic microscopy with improved sensitivity and speed, Optics letters 36 (7) (2011) 1134–1136.

[10] L. Wang, K. I. Maslov, W. Xing, A. Garcia-Uribe, L. V. Wang, Video-rate functional photoacoustic microscopy at depths, Journal of biomedical optics 17 (10) (2012) 106007.

[11] M.-L. Li, J. C. Wang, J. A. Schwartz, K. L. Gill-Sharp, G. Stoica, L. V. Wang, In-vivo photoacoustic microscopy of nanoshell extravasation from solid tumor vasculature, Journal of biomedical optics 14 (1) (2009) 010507.

[12] H. Zhong, T. Duan, H. Lan, M. Zhou, F. Gao, Review of low-cost photoacoustic sensing and imaging based on laser diode and light-emitting diode, Sensors 18 (7) (2018) 2264.

[13] T. J. Allen, P. C. Beard, Pulsed near-infrared laser diode excitation system for biomedical photoacoustic imaging, Optics letters 31 (23) (2006) 3462–3464.

[14] L. Zeng, G. Liu, D. Yang, X. Ji, Portable optical-resolution photoacoustic microscopy with a pulsed laser diode excitation, Applied physics letters 102 (5) (2013) 053704.

[15] T. Wang, S. Nandy, H. S. Salehi, P. D. Kumavor, Q. Zhu, A low-cost photoacoustic microscopy system with a laser diode excitation, Biomedical optics express 5 (9) (2014) 3053–3058.

[16] L. Zeng, G. Liu, D. Yang, X. Ji, Cost-efficient laser-diode-induced optical-resolution photoacoustic microscopy for two-dimensional/three-dimensional biomedical imaging, Journal of biomedical optics 19 (7) (2014) 076017.

[17] A. Hariri, A. Fatima, N. Mohammadian, S. Mahmoodkalayeh, M. A. Ansari, N. Bely, M. R. Avanaki, Development of low-cost photoacoustic imaging systems using very low-energy pulsed laser diodes, Journal of biomedical optics 22 (7) (2017) 075001.

[18] M. Erfanzadeh, P. D. Kumavor, Q. Zhu, Laser scanning laser diode photoacoustic microscopy system, Photoacoustics 9 (2018) 1–9.

[19] M.-L. Li, P.-H. Wang, Optical resolution photoacoustic microscopy using a blu-ray dvd pickup head, in: Photons Plus Ultrasound: Imaging and Sensing 2014, Vol. 8943, International Society for Optics and Photonics, 2014, p. 894315.

[20] L. Zeng, Z. Piao, S. Huang, W. Jia, Z. Chen, Label-free optical-resolution photoacoustic microscopy of superficial microvasculature using a compact visible laser diode excitation, Optics express 23 (24) (2015) 31026–31033.

[21] A. Hariri, J. Lemaster, J. Wang, A. S. Jeevarathinam, D. L. Chao, J. V. Jokerst, The characterization of an economic and portable led-based photoacoustic imaging system to facilitate molecular imaging, Photoacoustics 9 (2018) 10–20.

[22] M. Erfanzadeh, Q. Zhu, Photoacoustic imaging with low-cost sources; a review, Photoacoustics 14 (2019) 1–11.

[23] T. Allen, E. Zhang, P. Beard, Large-field-of-view laser-scanning or-pam using a fibre optic sensor, in: Photons Plus Ultrasound: Imaging and Sensing 2015, Vol. 9323, International Society for Optics and Photonics, 2015, p. 93230Z.

[24] T. J. Allen, O. Ogunlade, E. Zhang, P. C. Beard, Large area laser scanning optical resolution photoacoustic microscopy using a fibre optic sensor, Biomedical optics express 9 (2) (2018) 650–660.

[25] C. Kim, T. N. Erpelding, K. I. Maslov, L. Jankovic, W. J. Akers, L. Song, S. Achilefu, J. A. Margenthaler, M. D. Pashley, L. V. Wang, Handheld array-based photoacoustic probe for guiding needle biopsy of sentinel lymph nodes, Journal of biomedical optics 15 (4) (2010) 046010.

[26] M. Basij, Y. Yan, S. S. Alshahrani, H. Helmi, T. K. Burton, J. W. Burmeister, M. M. Dominello, I. S. Winer, M. Mehrmohammadi, Miniaturized phased-array ultrasound and photoacoustic endoscopic imaging system, Photoacoustics 15 (2019) 100139.

[27] R. Bitton, R. Zemp, J. Yen, L. V. Wang, K. K. Shung, A 3-d high-frequency array based 16 channel photoacoustic microscopy system for in vivo micro-vascular imaging, IEEE transactions on medical imaging 28 (8) (2009) 1190–1197.

[28] R. J. Zemp, R. Bitton, K. K. Shung, M.-L. Li, G. Stoica, L. V. Wang, Photoacoustic imaging of the microvasculature with a high-frequency ultrasound array transducer, Journal of biomedical optics 12 (1) (2007) 010501.

[29] R. J. Zemp, L. Song, R. Bitton, K. K. Shung, L. V. Wang, Realtime photoacoustic microscopy in vivo with a 30-mhz ultrasound array transducer, Optics express 16 (11) (2008) 7915–7928.

[30] L. Song, K. I. Maslov, K. K. Shung, L. V. Wang, Ultrasound-array-based real-time photoacoustic microscopy of human pulsatile dynamics in vivo, Journal of biomedical optics 15 (2) (2010) 021303.

[31] L. Song, K. Maslov, L. V. Wang, Multifocal optical-resolution photoacoustic microscopy in vivo, Optics letters 36 (7) (2011) 1236–1238.

[32] G. Li, K. I. Maslov, L. V. Wang, Multifocal optical-resolution photoacoustic microscopy in reflection mode, in: Photons Plus Ultrasound: Imaging and Sensing 2013, Vol. 8581, International Society for Optics and Photonics, 2013, p. 858126.

[33] P. Hajireza, W. Shi, P. Shao, S. Kerr, R. Zemp, Optical-resolution photoacoustic micro-endoscopy using image-guide fibers and fiber laser technology, in: Photons Plus Ultrasound: Imaging and Sensing 2011, Vol. 7899, International Society for Optics and Photonics, 2011, p. 78990P.

[34] F. Zheng, X. Zhang, C. T. Chiu, B. L. Zhou, K. K. Shung, H. F. Zhang, S. Jiao, Laser-scanning photoacoustic microscopy with ultrasonic phased array transducer, Biomedical optics express 3 (11) (2012) 2694–2698.

[35] J. R. Cook, R. R. Bouchard, S. Y. Emelianov, Tissue-mimicking phantoms for photoacoustic and ultrasonic imaging, Biomedical optics express 2 (11) (2011) 3193–3206.

[36] J. Park, S. Jeon, J. Meng, L. Song, J. S. Lee, C. Kim, Delay-multiply-and-sum-based synthetic aperture focusing in photoacoustic microscopy, Journal of biomedical optics 21 (3) (2016) 036010.

[37] M. Mozaffarzadeh, M. H. Varnosfaderani, A. Sharma, M. Pramanik, N. de Jong, M. D. Verweij, Enhanced contrast acoustic-resolution photoacoustic microscopy using double-stage delay-multiply-and-sum beamformer for vasculature imaging, Journal of biophotonics 12 (11) (2019) e201900133.

[38] G. Matrone, A. Ramalli, P. Tortoli, G. Magenes, Experimental evaluation of ultrasound higher-order harmonic imaging with filtered-delay multiply and sum (f-dmas) non-linear beamforming, Ultrasonics 86 (2018) 59–68.

[39] R. Paridar, M. Mozaffarzadeh, V. Periyasamy, M. Pramanik, M. Mehrmohammadi, M. Orooji, Sparsity-based beamforming to enhance two-dimensional linear-array photoacoustic tomography, Ultrasonics 96 (2019) 55–63.

[40] S. Shamekhi, V. Periyasamy, M. Pramanik, M. Mehrmohammadi, B. M. Asl, Eigenspace-based minimum variance beamformer combined with sign coherence factor: Application to linear-array photoacoustic imaging, Ultrasonics (2020) 106174.

[41] Z. Deng, X. Yang, H. Gong, Q. Luo, Adaptive synthetic-aperture focusing technique for microvasculature imaging using photoacoustic microscopy, Optics express 20 (7) (2012) 7555–7563.

[42] K. Nakahata, K. Karakawa, K. Ogi, K. Mizukami, K. Ohira, M. Maruyama, S. Wada, T. Namita, T. Shiina, Three-dimensional saft imaging for anisotropic materials using photoacoustic microscopy, Ultrasonics 98 (2019) 82–87.